Journal of
Materials Chemistry A

ROYAL SOCIETY
OF CHEMISTRY

PAPER

View Article Online
View Journal

Check for updates

Cite this: DOI: 10.1039/d6ta00742b

Amplified excited-state diverse effects arising from ligand regioisomerism in Cu(I) complexes for advanced applications

Cecilia Bruschi,†[a] Dominik Graf,[b] Olaf Fuhr,[bc] Valerio Cuboni,[d] Raffaella Lettieri,[d] Emanuela Gatto,[d] Sergei Lebedkin,[b] Angela Bihlmeier*[e] and Claudia Bizzarri*[ad]

Received 26th January 2026
Accepted 4th May 2026

DOI: 10.1039/d6ta00742b

rsc.li/materials-a

Designing earth-abundant photoactive coordination complexes that combine molecular tunability with device-relevant performance is essential to advance next-generation optoelectronic and solar-energy technologies. In this work, two heteroleptic Cu(I) complexes were synthesised using regioisomeric diimine ligands obtained through lactam–lactim tautomerism of a common precursor. Despite their close structural similarity, the complexes exhibit pronounced differences in photophysical and electrochemical behaviour. In the solid state, both compounds show phosphorescent emission, whereas at room temperature one complex displays some characteristics consistent with thermally activated delayed fluorescence. Quantum-chemical calculations reveal a rather large singlet–triplet energy gap for the charge-transfer states, and a ligand-centred triplet state is supposed to play a decisive role. Preliminary photoelectrochemical measurements further demonstrate that simple physisorption of the complexes onto TiO_2 yields measurable photocurrent generation. These results highlight the significant impact of ligand regiochemistry on the excited-state properties and functional performance of Cu(I) complexes.

Introduction

The quest for cost-effective functional materials that are easy to prepare and accessible is strongly encouraged by the need to stop relying on expensive metals and increase the sustainability of the targeted application. Metal coordination compounds are a fascinating class of materials that find application in almost every field depending on their design, metal core and oxidation state, and ligand scaffold. Among the earth-abundant-based possibilities,[1,2] coordination complexes based on Cu(I) are the most studied alternatives to expensive and rare transition metal complexes (*e.g.* Ir, Ru, Pt) for photophysical applications, thanks to their higher abundance in the earth's crust, limited costs, and versatile chemistry. Typically, their photoactivity is derived from the lowest excited state, which is metal-to-ligand charge-transfer (MLCT) in character, with the metal-centred transitions prevented by the d^{10} electronic configuration of Cu(I). Although the spin–orbit coupling (SOC) is moderate, triplet excited states can also be populated. In fact, several Cu(I) complexes allow not only efficient intersystem crossing (ISC) processes, but also reverse ISC, when a minimal gap between the singlet and the triplet states is present (usually < 0.2 eV), showing thermally-activated delayed fluorescence (TADF).[3] The TADF characteristics are attractive not only for luminescent dopants for organic light-emitting devices (OLEDs) or light-emissive electrochemical cells (LECs), assuring harvesting of both S and T states, but also in photocatalysis,[4,5] although this application is mainly explored with TADF-emitters of organic nature, rather than organometallic ones. Copper complexes have found a principal role also as light-harvesting antennae,[6–9] as photosensitizers in photoelectrodes for dye-sensitized solar cells (DSSC),[10–16] and as photocatalysts.[17–22] Engineering of the organic (chelating) ligands becomes, therefore, very important to tune the energetic levels of the molecular orbitals of the copper complexes according to their purpose.[23] Thus, it is well-documented how structural variations in diimine or diphosphine ligands influence the photo- and electrochemical response.[24–27] Systematic investigations on how regioisomerism controls excited-state behaviour are well established for purely organic luminophores, where sets of regioisomers have revealed pronounced effects on TADF,[28–30] aggregation-induced emission,[31] solid-state colour tuning,[32,33] and

---

[a] *Institute of Organic Chemistry (IOC), Karlsruhe Institute of Technology (KIT), Fritz-Haber-Weg 6, 76131 Karlsruhe, Germany*

[b] *Institute of Nanotechnology (INT), Karlsruhe Institute of Technology (KIT), Hermann-von-Helmholtz-Platz 1, 76344 Eggenstein-Leopoldshafen, Germany*

[c] *Karlsruhe Nano Micro Facility (KNMFi), Karlsruhe Institute of Technology (KIT), Hermann-von-Helmholtz-Platz 1, 76344 Eggenstein-Leopoldshafen, Germany*

[d] *Department of Chemical Sciences and Technologies, University of Rome Tor Vergata, Via Della Ricerca Scientifica, 00133 Rome, Italy. E-mail: claudia.bizzarri@uniroma2.it*

[e] *Institute of Physical Chemistry (IPC), Karlsruhe Institute of Technology (KIT), Fritz-Haber-Weg 2, 76131 Karlsruhe, Germany. E-mail: angela.bihlmeier@kit.edu*

† Present Address: Linköping University, Department of Science and Technology, Bredgatan 33, 60221 Norrköping, Sweden.

photocatalysis.[34–36] By contrast, analogous studies of the structure-photophysical behaviour based on regioisomeric ligands are much rarer for Cu(I) complexes,[37–41] and essentially absent when the regioisomers arise from a keto–enol or lactam–lactim tautomeric equilibrium at the ligand-synthetic stage. While protonation–deprotonation and related prototropic equilibria in ligands have been shown to markedly affect the emission of coordination complexes based on Cu(I) in a few selected systems,[42–44] the explicit use of keto–enol tautomerism to tune the excited states of these complexes remains mostly discussed in terms of structural chemistry[45] or in the emission of organic-based molecules.[46] Consequently, we intend to fill this gap with the present work, specifically addressing how much tautomerism-derived regioisomerism perturbs the interplay of the excited states in luminescent Cu(I) complexes. In particular, we show two novel heteroleptic Cu(I) complexes that have diimine ligands, which differ only by the position of an ethyl substituent. This ethyl group is linked to a nitrogen atom in one isomer and to an oxygen atom in the other isomer, because of the ethylation of the lactam (keto-amine, **k**) and the lactim (enol-imine, **e**) tautomers, respectively, of the 3-(triisopropyl)ethynylquinoxalin-2-one precursor of the chelating ligands. Interestingly, these regioisomeric complexes display markedly distinct excited-state behaviour. In addition to a variance of the photophysics and electrochemistry in solution, induced by the energetic landscape of the two diimines, intriguing behaviour was revealed by low-temperature solid-state photoluminescence, complemented by DFT calculations. Our theoretical studies support the involvement of a ligand-centred triplet excited state (LE), which is energetically accessible only in one regioisomer, interplaying between singlet and triplet MLCT. Finally, we present preliminary photocurrent results of these two complexes, physically adsorbed on a TiO_2 surface. The cathodic and anodic photocurrent could be generated through variation of the donor/acceptor environment and the applied potential, in both regioisomers, highlighting how the diverse energetics of the two complexes is reflected in their photocurrent efficiency.

Results and discussion

Synthetic procedures and characterisation

The first step of the synthetic procedure for the ligands is a condensation reaction between *ortho*-diaminobenzene and methyl 2-oxo-4-(triisopropylsilyl)but-3-ynoate,[47] in a mixture of ethanol and glacial acetic acid (7 : 3, v/v), refluxed at 80 °C overnight.[48] The product was obtained after extraction and removal of solvent by rotatory evaporation under reduced pressure. The solid light-yellow compound corresponds to the 3-((triisopropylsilyl)ethynyl)quinoxalin-2(1*H*)-one (2), which is the most stable tautomeric form of the lactam–lactim tautomerism (Scheme 1).

Nevertheless, the lactim form is stable enough to react besides the lactam form with ethyliodide in *N*,*N*-dimethylformamide (DMF) in the presence of a base (K_2CO_3) at 50 °C. After two hours, two products in a 2 : 1 ratio were isolated from the purification of the reaction mixture: 1-ethyl-3-((triisopropylsilyl)ethynyl)quinoxalin-2(1*H*)-one (**3k**) resulted from the reaction with the keto-amine (*i.e.* lactam) tautomer, and 2-ethoxy-3-((triisopropylsilyl)ethynyl)quinoxaline (**3e**) resulted from the reaction of the enol-imine (*i.e.* lactim) tautomer. Their chemical structures were confirmed by ^{1}H and ^{13}C NMR spectroscopy and by X-ray analysis of the crystal of the ethoxy derivative (see Fig. S9 in the SI). The synthesis of the final ligands proceeded in parallel using the same conditions for both regioisomers. Thus, after removal of the TIPS group with tetrabutylammonium fluoride (TBAF), the terminal alkynes could react further with benzylazide *via* a copper-catalysed azide–alkyne cyclization reaction (CuAAC).[49] Purification through flash-chromatography on silica gel gave the desired products 3-(1′-benzyl-1′*H*-1′,2′,3′-triazol-4′-yl)-1-ethylquinoxalin-2(1*H*)-one (**4k**) and 2-(1′-benzyl-1′*H*-1′,2′,3′-triazol-4′-yl)-3-ethoxyquinoxaline (**4e**), respectively with final yields of 70% and 91%.

The heteroleptic Cu(I) complexes **5k** and **5e** (Fig. 1) were synthesised from ligands **4k** and **4e** respectively, following our well-established procedure, employing DPEPhos as the chelating diphosphine and $[Cu(NCCH_3)_4]PF_6$ as the Cu(I)

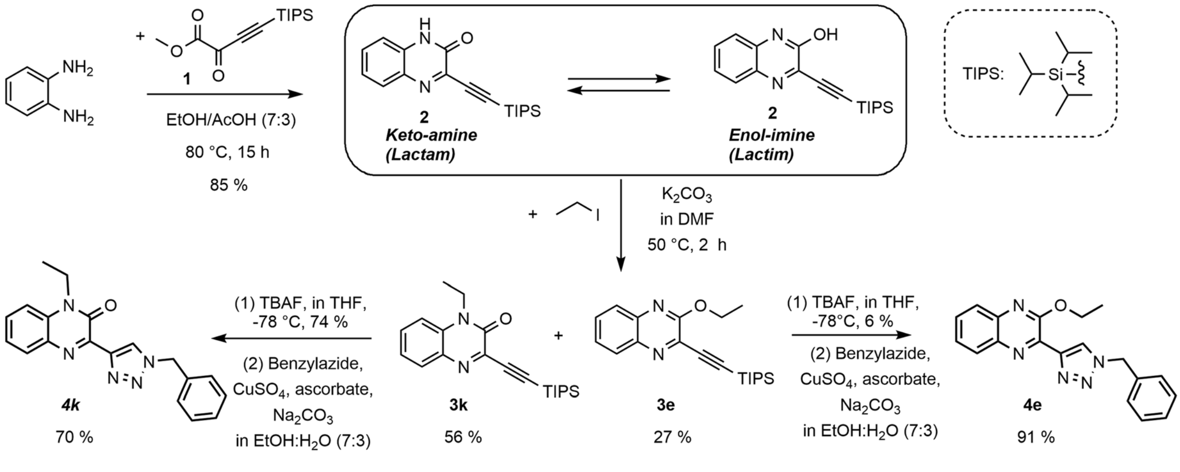

Scheme 1 Synthetic procedures for the ligands **4k** and **4e**.

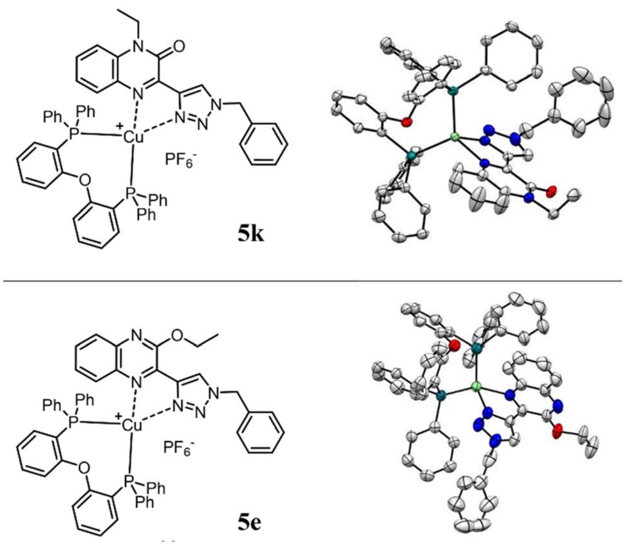

Fig. 1 Chemical structures (left) and ORTEP drawings of the crystals (right) of the heteroleptic Cu(I) complexes **5k** (top) and **5e** (bottom).

precursor.[18,43] The isolated Cu(I) complexes grew high quality crystals, by diffusion of a cyclohexane layer (placed atop) into their concentrated solutions in dichloromethane (DCM). The crystal structures of the two regioisomeric complexes belong to two different systems. While the crystal structure of complex **5e** belongs to the triclinic system with a $P\bar{1}$ space group, the crystal structure of **5k** belongs to the monoclinic system with a $P2_1/c$ group. However, their bond lengths and bite angles are similar. In fact, the distances between the copper centre and the nitrogen atom of the triazole ring (Cu–N3) are: 2.066 Å and 2.048 Å for **5k** and **5e**, respectively, which are smaller than the those between the copper and the nitrogen atom of the quinoline ring (Cu–N1): 2.084 Å for **5k**, 2.122 Å for **5e**. In both complexes, the bond distances between the metal centre and the coordinative P atoms of the DPEPhos are alike to each other (Cu–P1: 2.244 Å for **5k**, 2.250 Å for **5e**; Cu–P2: 2.232 Å for **5k**, 2.243 Å for **5e**), as well as are their bite angles N1–Cu–N3 (79.55° for **5k**, 79.68° for **5e**) and P1–Cu–P2 (112.49° for **5k**, 111.09° for **5e**).

Photophysical characterisation

The stability of both complexes in polar solvents, such as DCM and acetonitrile (ACN), was tested by ^{1}H NMR spectroscopy and UV-vis spectroscopy over a period of a week (see Fig. S11–S13). Therefore, characterisation was performed with these solvents. The two Cu(I) complexes show distinct UV-vis absorption spectra (Fig. 2a), indicating a profound influence of the regioisomeric quinoxaline ligands on their electronic structure. Well-structured absorption bands are observed below the onset at *ca.* 530 nm (**5k**) and 500 nm (**5e**), with molar extinction coefficients of *ca.* 1×10^4 M^{-1} cm^{-1} between 350 nm and 500 nm and 5×10^4 M^{-1} cm^{-1} at 230 nm for both complexes. In fact, their absorption spectra within the range of 300–400 nm reflect the profiles of the respective regioisomeric ligands **4k** and **4e** (see Fig. S14). Accordingly, the absorption bands of both complexes in that region are mainly attributed to ligand-centred transitions in those ligands, whereas the lowest energy bands at the absorption onsets are assigned to metal-to-ligand charge-transfer (MLCT) transitions. This assignment is supported by our quantum-chemical calculations (see below). In DCM solution, complexes **5k** and **5e** show moderately bright red photoluminescence (PL) with a maximum at 743 nm and 700 nm (Fig. 2b), and a lifetime of 36 ns and 180 ns, respectively (the latter parameters were measured in solutions under an argon atmosphere). The emission bands are quite broad, which is typical for charge-transfer transitions. In contrast, moderately bright emission of the ligands in DCM solution occurs in the blue spectral region at *ca.* 425 nm (**4k**) and 390 nm (**4e**). Their emission spectra roughly mirror the excitation (absorption) profiles, show some vibronic features, and can be ascribed to the ligand fluorescence (Fig. S15 and S16).

Photoluminescence of the two regioisomeric complexes was also investigated in the solid (polycrystalline) state (Fig. 3). Similarly to what was observed in solutions at room temperature, the solid-state emission of **5k** shows a broad profile centred at 681 nm, *i.e.* red-shifted by about −0.15 eV as compared to the emission of **5e**, centred at 628 nm (Fig. 3). The hypsochromic shifts of these emissions with regard to the respective luminescence in solution are due to rigidochromism. The

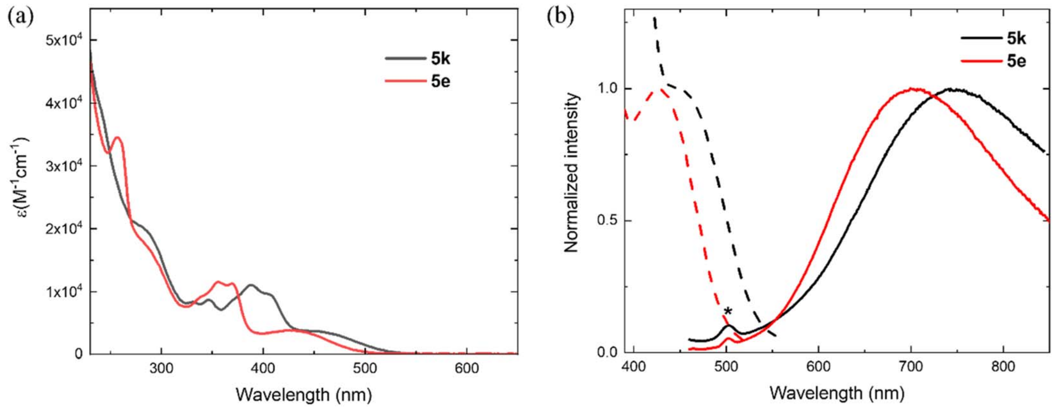

Fig. 2 (a) UV-vis absorption spectra, and (b) excitation (dashed) and emission (solid) of the Cu(I) complexes **5k** (black) and **5e** (red) in dichloromethane (* marks the Raman contribution of the solvent when exciting at 445 nm).

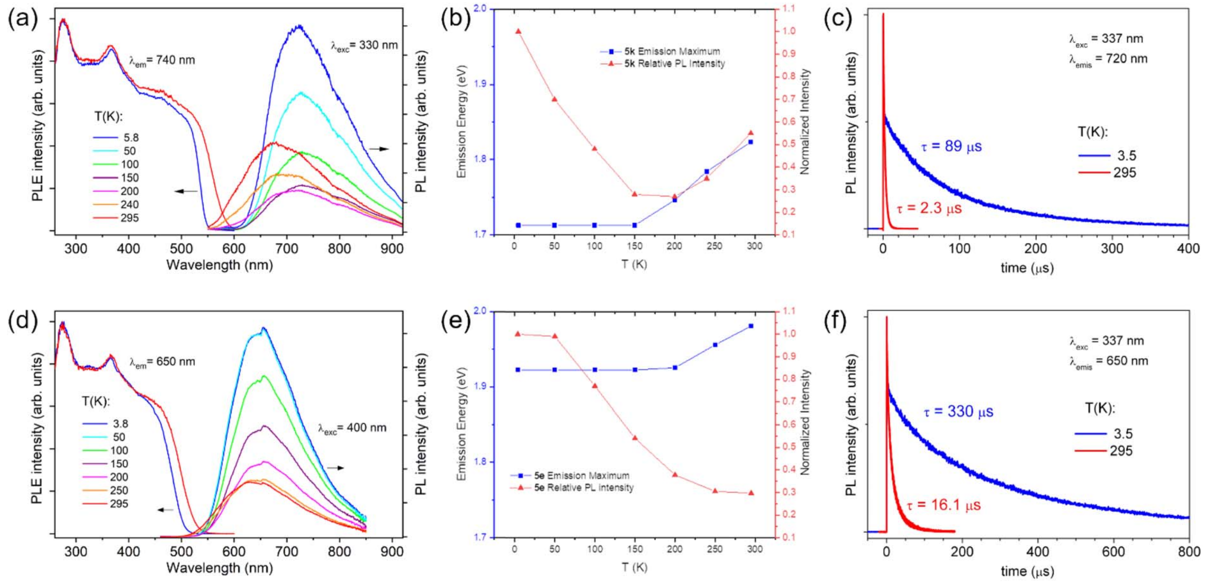

Fig. 3 (a) Excitation (left) and emission (right) of the polycrystalline sample **5k** in the temperature range of 5.8 K to 295 K. (b) Correlation of the normalized photoluminescence area and the maximum emission energy for **5k**. (c) Lifetime decay of **5k** excited state at $T = 295$ K (red curve) and $T = 3.5$ K (blue curve). (d) Excitation (left) and emission (right) of the polycrystalline sample **5e** in the temperature range of 3.8 K to 295 K. (e) Correlation of the normalized photoluminescence area and the maximum emission energy for **5e**. (f) Lifetime decay of **5e** excited state at $T = 295$ K (red curve) and $T = 3.5$ K (blue curve).

quantum yield recorded for **5k** is 3.1%, while it is about three times higher for **5e** (9.9%). Surprisingly, the two Cu(I) regioisomers also show a different behaviour by decreasing the temperature. By cooling below 10 K, the emission spectra are bathochromically shifted to 644 nm ($\Delta E = 0.05$ eV) and 724 nm ($\Delta E = 0.11$ eV) for **5e** and **5k**, respectively, and the PL intensity is notably enhanced, indicating reduction of non-radiative decay pathways, allowing the spin–orbit coupling to play a more prominent role in the excited-state dynamics and effectively stabilizing the triplet states. Therefore, taken separately, the bathochromic shift of less than 0.2 eV observed upon cooling would match the typical feature of a TADF mechanism, initially suggesting that the room-temperature emission arises from a higher-lying singlet excited state, populated *via* reverse intersystem crossing (RISC), consistent with reports on other Cu(I) complexes.[50–54] However, while complex **5e** exhibits a continuous increase in the photoluminescence intensity (PL) by lowering the temperature, the case of complex **5k** is more complicated. Indeed, by going from 295 K to 200 K, the emission spectrum of **5k** is bathochromically shifted from 681 nm to about 700 nm, but the luminescence intensity is decreased. By further cooling the sample from 200 K down to 5.8 K, the emission spectra are further red-shifted to 724 nm, while the intensity increases (see Fig. 3b and e for **5k** and **5e**, respectively).

The different behaviours of **5e** and **5k** are also evident when observing the excited-state lifetimes (see Fig. S18 and S19). These were determined from biexponential/monoexponential fits of PL decays of **5e**/**5k** (excited by a ns-pulsed laser at 337 nm) as 16.1 μs (average lifetime) and 2.3 μs, respectively, at a temperature of 295 K. These values roughly correlate with the PL quantum yields, indicating more efficient non-radiative relaxation in **5k** than in **5e**. In turn, the latter likely correlates with the lower energy of absorption and emission transitions (lower band gap) observed in the **5k** regioisomer. By decreasing the temperature to about 3.5 K, the PL lifetimes increase significantly to 89 μs and 330 μs for **5k** and **5e**, respectively,

Table 1 Photophysical data of the Cu(I) complexes **5k** and **5e**, recorded in Ar-saturated dichloromethane solutions and in the solid state

	Solution			Solid state				
	298 K			295 K			3.5 K	
	λ_{abs}/nm	λ_{em}/nm	τ/ns[a]	λ_{em}/nm	τ/μs[b]	Φ[c]	λ_{em}/nm	τ/μs[b]
5k	276, 331, 346, 370, 388, 406, 460	743	36	681	2.3	0.031	724	89
5e	257, 285, 338, 355, 369, 427	700	180	628	16.1	0.099	644	330

[a] Lifetimes in solution at room temperature were recorded with a time-correlated single-photon-counting and with Nanoled as excitation source ($\lambda_{exc} = 368$ nm). [b] Lifetimes in the solid state were recorded by connecting a photomultiplier to a fast oscilloscope and using a nitrogen laser (~2 ns, ~5 μJ per pulse) for pulsed excitation at 337 nm. [c] PLQY values in the solid state were measured at 298 K using an integrating sphere.

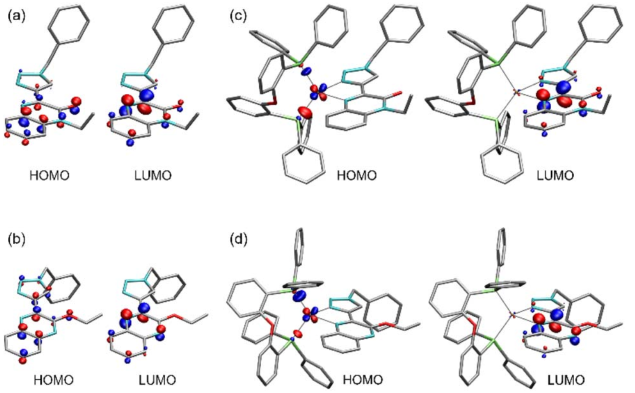

Fig. 4 HOMO and LUMO of the ligands (a) **4k** and (b) **4e** as well as of the corresponding Cu(I) complexes (c) **5k** and (d) **5e** at their respective ground state geometries (isovalue ±0.1 bohr$^{-3/2}$). Hydrogen atoms are omitted for clarity.

corresponding to factors of roughly 40 and 20. However, this increase occurs nearly monotonously for both compounds, with the exception of slight irregularities between 100 K and 200 K (Fig. S20). The long-lived low-temperature emission of **5k** and **5e** can definitely be assigned to phosphorescence. The emission may also preserve the same character at ambient temperature. On the other hand, taking into account the somewhat peculiar temperature dependences of the PL lifetime, intensity, and emission spectra, especially for **5k**, one may consider a possible contribution of the singlet excited state at elevated temperature above 200 K. A TADF process depends on a sufficiently small energy gap (usually <0.2 eV) between the relaxed S_1 and T_1 states. However, the experimental evidence for TADF in **5k** and **5e** is limited so far. One TADF signature is, for instance, a characteristic reverse S-shape temperature dependence of the PL lifetime. This could not be clearly observed in **5k** and **5e**, as a strong temperature dependence of non-radiative relaxation of the excited states mainly determines the decrease of the PL lifetime in **5k** and **5e** when increasing the temperature. The summary of the photophysical properties for complexes **5k** and **5e** is presented in Table 1.

Quantum-chemical calculations

In order to gain further insight into the observed differences between the lactam- and the lactim-based structures, quantum-chemical calculations were performed for both the ligands and the Cu(I) complexes.

Fig. 4 shows the highest occupied (HOMO) and the lowest unoccupied molecular orbitals (LUMO) of the ligands **4k** and **4e** as well as of the Cu(I) complexes **5k** and **5e**. The LUMO of the ligands and the corresponding LUMO of the complexes are virtually identical.

The simulated absorption spectra (see Fig. S21 and S22) show a red shift for the lactam-based structures **4k** and **5k**, which is in line with the measured UV-vis spectra. The lower excitation energy of **4k** compared to **4e** (Table S2) arises from a smaller HOMO–LUMO gap, where the HOMO of **4k** is shifted to higher energies and the LUMO is shifted to lower energies. For **5k** and **5e**, the first excitation corresponds to a HOMO–LUMO transition (see Table S3), where the HOMO is located on the metal while the LUMO is located on the ligand (^{1}MLCT state). Thus, the smaller excitation energy of **5k** is directly connected to the LUMO of **4k** being lower in energy than the LUMO of **4e**.

Table 2 Excitation energies of the three lowest singlet and triplet excitations of **5k** and **5e** at the optimised ^{1}MLCT geometry. The excitations S_1 and T_1 correspond to metal-to-ligand charge-transfer states (^{1}MLCT and ^{3}MLCT), while T_2 corresponds to a local triplet state on the ligand (^{3}LE)

	E (eV)	Dominant contribution		E (eV)	Dominant contribution
5k					
S_1	2.23	88.4% H → L	T_1	2.08	81.5% H → L
S_2	3.32		T_2	2.14	85.2% H−2 → L
S_3	3.47		T_3	2.91	
5e					
S_1	2.34	88.4% H → L	T_1	2.20	84.6% H → L
S_2	3.67		T_2	2.69	53.3% H−3 → L
S_3	3.71		T_3	2.90	

For a better understanding of the photophysical processes that could occur upon excitation, the geometries of the ^{1}MLCT and ^{3}MLCT states of **5k** and **5e** were also optimised. Values of selected bond lengths and bond angles and how they are changing in the different geometries are summarised in Tables S4–S7. With respect to the ground state, the ^{1}MLCT and ^{3}MLCT states of **5k** and **5e** show longer Cu–P and shorter Cu–N bond distances, leading to slightly different bite angles. Besides, a longer C–N bond distance in the coordinated quinoxaline ligand is found. The CT states themselves do not differ much. Going from the ^{1}MLCT state to the ^{3}MLCT state essentially results in a shorter Cu–P bond and a shorter Cu–N bond. Furthermore, also the singlet and triplet excitation energies at the optimised charge-transfer geometries were computed (Tables 2 and 3). In the following, we focus on the three energetically lowest excited states, that is, S_1, T_1, and T_2.

Table 3 Excitation energies of the three lowest singlet and triplet excitations of **5k** and **5e** at the optimised ^{3}MLCT geometry. The excitations S_1 and T_1 correspond to metal-to-ligand charge-transfer states (^{1}MLCT and ^{3}MLCT), while T_2 corresponds to a local triplet state on the ligand (^{3}LE)

	E (eV)	Dominant contribution		E (eV)	Dominant contribution
5k					
S_1	2.37	88.0% H → L	T_1	1.96	62.4% H → L
S_2	3.33		T_2	2.24	61.5% H−2 → L
S_3	3.39		T_3	2.90	
5e					
S_1	2.45	86.7% H → L	T_1	2.17	81.1% H → L
S_2	3.55		T_2	2.69	68.4% H−3 → L
S_3	3.61		T_3	2.91	

The difference between the electron density of the ground state and the selected excited states is depicted in Fig. S23 for **5k** and Fig. S24 for **5e**. The pair of natural transition orbitals (NTO) that describes the electron and the hole of the respective excitation is also given. Further, we have computed the quantity Λ that is used to measure the degree of spatial overlap between this pair of NTOs, and thus, the degree of charge transfer (see Table S8).[55] Based on these results, S_1 and T_1 can be verified as the ^{1}MLCT and ^{3}MLCT states mentioned above, while T_2 corresponds to a π–π* triplet excited state located on the ligand (^{3}LE).

The energetic ordering of the excited states at the different geometries (S_0, ^{1}MLCT and ^{3}MLCT) of **5k** and **5e** is displayed in Fig. 5. The most notable difference between the lactam- and the lactim-based Cu(I) complexes is found for the optimised charge-transfer geometries. In case of **5e**, both CT states (^{1}MLCT and ^{3}MLCT) shift below the ^{3}LE state, while for **5k**, the local triplet excited state is in between the ^{1}MLCT and ^{3}MLCT states. The singlet-triplet energy gaps, usually taken as a measure of the probability of reverse ISC (RISC) and thus TADF, were estimated for the CT states using different approximations (see Table S9). They are small at the ^{1}MLCT geometry and naturally become larger at the ^{3}MLCT geometry. In general, the values are rather in the upper range for a possible TADF process. Also, they are a little larger for **5k** than for **5e**.

To summarise, based on the results of the quantum-chemical investigations, the observed photophysical properties could be rationalised as follows. Upon excitation, both **5k** and **5e** relax to the lowest singlet excited state, ^{1}MLCT. This state is energetically and geometrically very close to the ^{3}MLCT state, thus enabling an efficient ISC process and relaxation to the ^{3}MLCT geometry. It is very likely that, at low temperatures, phosphorescence from this state is the main source of the observed luminescence. The energy of the $T_1 \rightarrow S_0$ transition is about 0.2 eV smaller for **5k** than for **5e** (Table 3), which is consistent with the experimentally observed wavelengths for the respective luminescence (724 nm for **5k** and 644 nm for **5e**, at 3.5 K). At higher temperatures, the computed values for the singlet-triplet energy gaps between the CT states suggest that RISC, and, thus TADF, is not very likely to occur, but is not excluded. This would be a suitable explanation for the experimentally observed behaviour of **5e**, where the luminescence intensity is reduced and only slightly blue-shifted when increasing the temperature (Fig. 3e). In contrast, **5k** shows an increase in the luminescence intensity above 200 K, connected with a more pronounced blue shift (Fig. 3b). Since the main difference observed in the computations is the energetics of the local triplet excited state, it is reasonable to assume that this state might be predominantly responsible for the peculiar behaviour of **5k** in contrast to **5e**. Two possible explanations are suggested in the following.

As the estimated CT singlet-triplet energy gap itself does not justify an efficient RISC process followed by TADF (or at least, not more efficient than that in the case of **5e**), we suspect that the local triplet excited state on the ligand could possibly play a role here and enhance RISC for **5k**. The circumstance that an efficient RISC process not only requires a small singlet-triplet energy gap but also an energetically close local triplet state has been proposed and discussed in the literature.[56–58] Instead of the spin–orbit coupling between the two CT states (which is

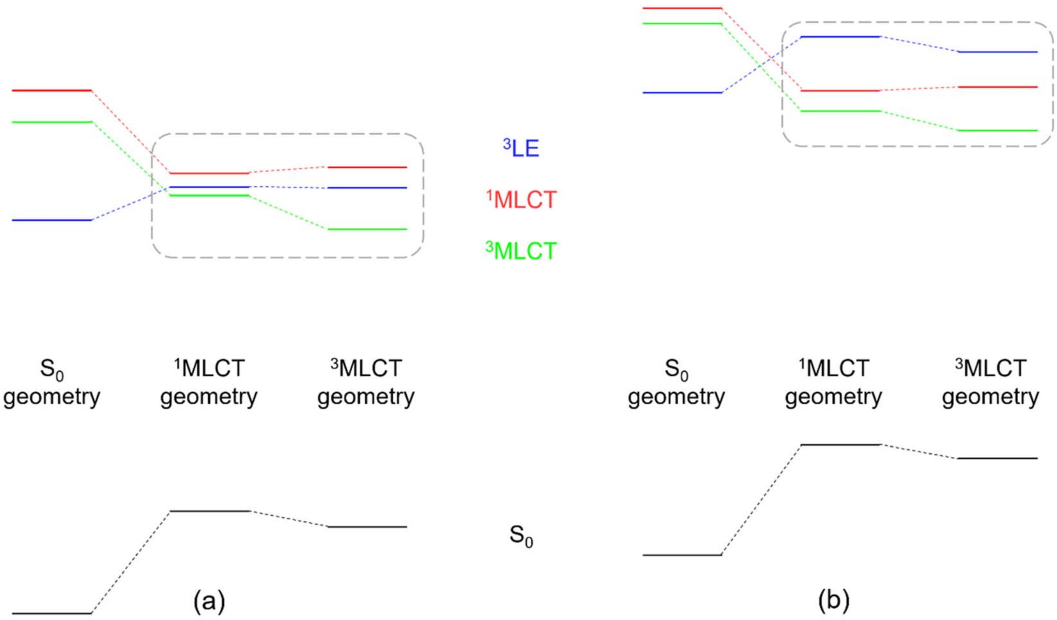

Fig. 5 Energetic ordering of the metal-to-ligand charge-transfer singlet and triplet states (^{1}MLCT and ^{3}MLCT) and the local triplet excited state on the ligand (^{3}LE) at different optimised geometries of (a) **5k** and (b) **5e**. The most notable difference is found for the optimised charge-transfer geometries: for **5e**, both ^{1}MLCT and ^{3}MLCT shift below the local triplet state, whereas for **5k**, the local triplet state is in between ^{1}MLCT and ^{3}MLCT.

Table 4 Electrochemical data of the Cu(I) complexes **5k** and **5e**, recorded in dichloromethane[a] and acetonitrile[b] solutions (0.1 M $TBAPF_6$) reported *versus* Fc/Fc^+.[c]

Sample	E_{ox}/V	E_{red}/V	ΔE_{el}/V	E_{HOMO}/eV	E_{LUMO}/eV	E_{00}/eV[d]	E^*_{ox}/V	E^*_{red}/V
5k	1.08[a] 0.85[b]	−1.57[a] −1.49[b] −2.29[b]	2.65[a] 2.34[b]	−6.18[a] −5.95[b]	−3.53[a] −3.61[b]	2.35[a] 2.42[b]	−1.27[a] −1.57[b]	0.78[a] 0.93[b]
5e	1.02[a] 0.88[b]	−1.73[a] −1.71[b] −2.58[b]	2.75[a] 2.59[b]	−6.12[a] −5.98[b]	−3.37[a] −3.39[b]	2.47[a] 2.52[b]	−1.45[a] −1.64[b]	0.74[a] 0.81[b]

[a] Obtained in a 2 mM DCM solution with 0.1 M $TBAPF_6$, at room temperature. [b] Obtained in a 2 mM ACN solution with 0.1 M $TBAPF_6$, at room temperature. [c] To calculate the values *versus* NHE, 0.64 V must be added.[60] [d] E_{00} has been estimated by the onset wavelength of the MLCT absorption peak.[61]

similar for **5k** and **5e**), a second-order term involving the ^{3}LE state would be important in the case of **5k**. Alternatively, the ^{3}LE state could be populated at higher temperatures, followed by emission from this state. Both of these scenarios could explain the blue shift in the emission maximum and the increase in the PL intensity when increasing the temperature above 200 K, with TADF being the more probable explanation. On the other hand, the strong and monotonous decrease of the PL lifetime with increasing temperature cannot yet be fully rationalized in this context. Future in-depth photophysical analyses are expected to clarify the underlying processes.

Electrochemistry

Cyclic voltammetry (CV) was recorded employing an electrochemical cell of three-electrodes, under an argon atmosphere, in a solution of methylene chloride (DCM) or acetonitrile (ACN) with 0.1 M tetrabutylammonium hexafluorophosphate ($TBAPF_6$) as the supporting electrolyte. The CV of ligands **4e** and **4k** was measured only in DCM (0.1 M $TBAPF_6$). All redox potentials are reported *versus* the Ferrocene/Ferrocenium pair (Fc/Fc^+), according to the IUPAC indication,[59] and listed in Table 4. The two copper complexes **5k** and **5e** present oxidation at *ca.* 1.0 V, which is attributed to the oxidation of the copper centre Cu(I)/Cu(II). Interestingly, while the oxidation of the complex **5k** is irreversible, the oxidation signal of **5e** is quasi-reversible, as the cathodic current is more pronounced (Fig. 6). In contrast, the reduction signals are reversible for both heteroleptic copper complexes. In the cathodic scan, **5k** is reduced at −1.57 V, which is at higher potential ($\Delta V \approx 0.15$ V) compared to the reduction process of **5e**, recorded at −1.73 V. When recorded in acetonitrile, the electrochemical window of the solvent allows to also detect a second reduction process that is irreversible and appearing at −2.29 V and −2.58 V for **5k** and **5e**, respectively.

The electrochemical gap between the oxidation and the first reduction (ΔE_{el}) can be associated with the HOMO–LUMO gap and follows the same trend observed in the photophysical characterisation and theoretical investigation. In fact, ΔE_{el} for **5k** is 2.65 V in DCM and 2.34 V in ACN; while for **5e** it is 2.75 V in DCM and 2.59 V in ACN. The decrease of ΔE_{el} in ACN is usually observed for compounds where the excited state has a polar nature, as this is the case for the Cu(I) complexes (MLCT state). The first oxidation and the first reduction correlate with the HOMO and LUMO energies, and their estimation was done considering the potential values *versus* ferrocene adding 5.1 eV.[60]

Photoelectrochemical studies

Given the promising photophysical and electrochemical features of the two Cu(I) complexes, we carried out photocurrent generation experiments on both compounds after deposition onto conductive surfaces. The two Cu(I) complexes **5k** and **5e** have been deposited onto a TiO_2/FTO surface, by dropping 20

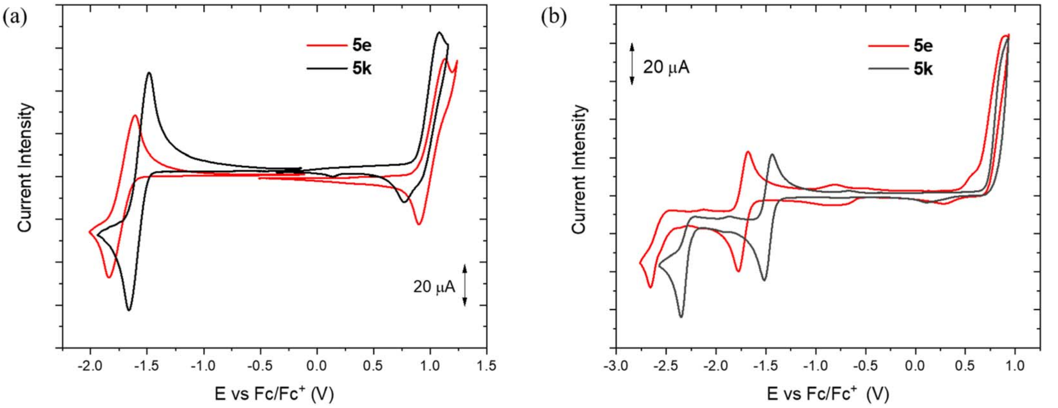

Fig. 6 Cyclic voltammetry of **5e** (red curve) and **5k** (black curve) in a 2 mM solution of (a) DCM (0.1 M $TBAPF_6$) and (b) ACN (0.1 M $TBAPF_6$).

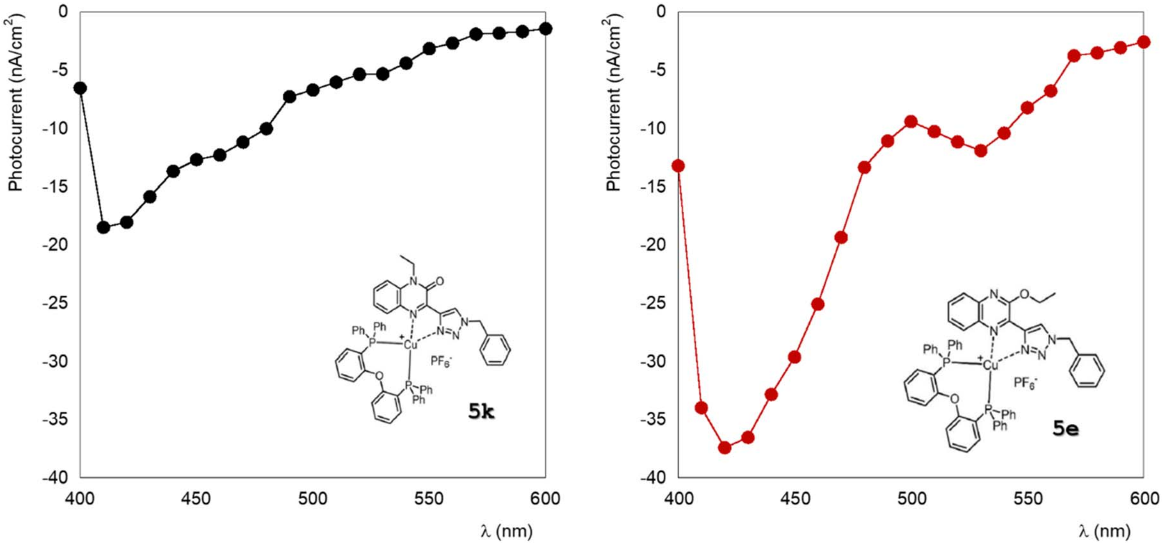

Fig. 7 Photocurrent action spectra of film **5k** (left) and **5e** (right) on TiO_2/FTO electrodes. The measurements were performed in an aqueous TEOA solution, at 0 V (*vs.* Ag/AgCl), upon photoirradiation at different wavelengths (every 10 nm from 400 to 600 nm).

μL of a 0.2 mM acetonitrile solution onto the TiO_2 substrate and letting it dry for one hour before analysis. In general, TiO_2 substrates, characterised by a low-energy conduction band, act as photoanodes, that is, the surface onto which photoexcited electrons are injected, thereby generating an anodic photocurrent.

In the presence of an electron-donating solution, such as 50 mM aqueous triethanolamine (TEOA), a pronounced anodic photocurrent is observed in the UV region. This behaviour can be attributed to the intrinsic absorption of titanium dioxide within this wavelength range (see Fig. S26). In contrast, in the visible region the signal reverses to a negative (cathodic) photocurrent, indicating that the system behaves as a photocathode. This behaviour is consistently observed for complexes **5k** and **5e**. Above 400 nm, the action spectra, that is, the photocurrent response graphs as a function of excitation wavelength, display a marked increase in correspondence with the absorption bands of the two complexes (Fig. 7). This observation confirms that the Cu(I) complexes are responsible for the cathodic photocurrent observed in this spectral range. Moreover, the wavelengths of maximum photocurrent generation closely match the main absorption maximum of the complexes in solution.

The cathodic response observed for complexes **5k** and **5e** in an electron-donor medium such as triethanolamine may arise from their low excited-state oxidation potentials, which are very close to the edge of the conduction band of the TiO_2 substrate (Fig. 8). The conduction and valence band values of TiO_2 have

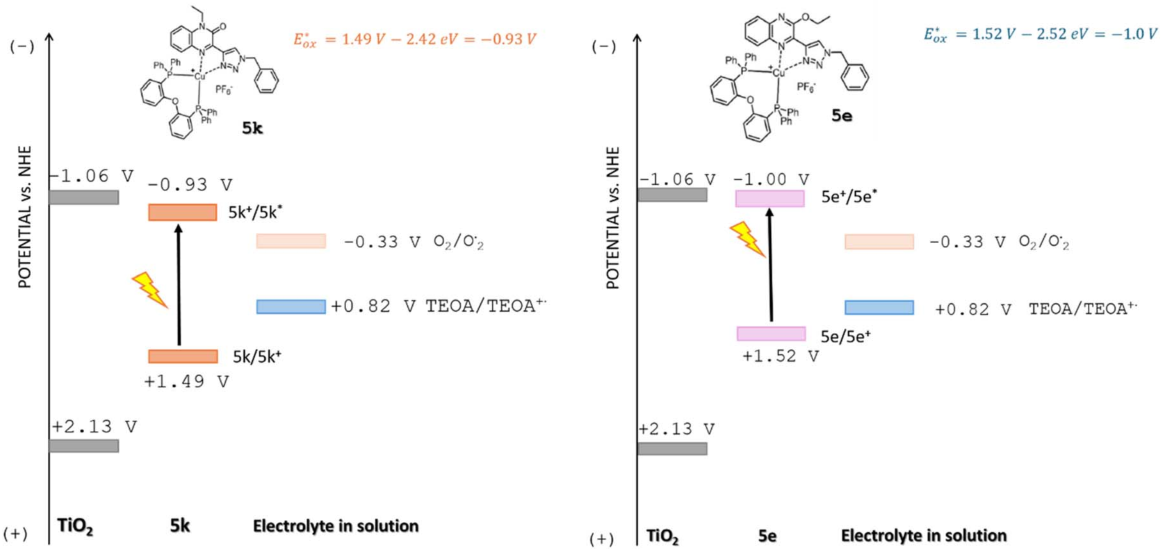

Fig. 8 Schematic representation of the energy levels *versus* NHE involved in the photocurrent process in TEOA solution, at pH = 9.6.

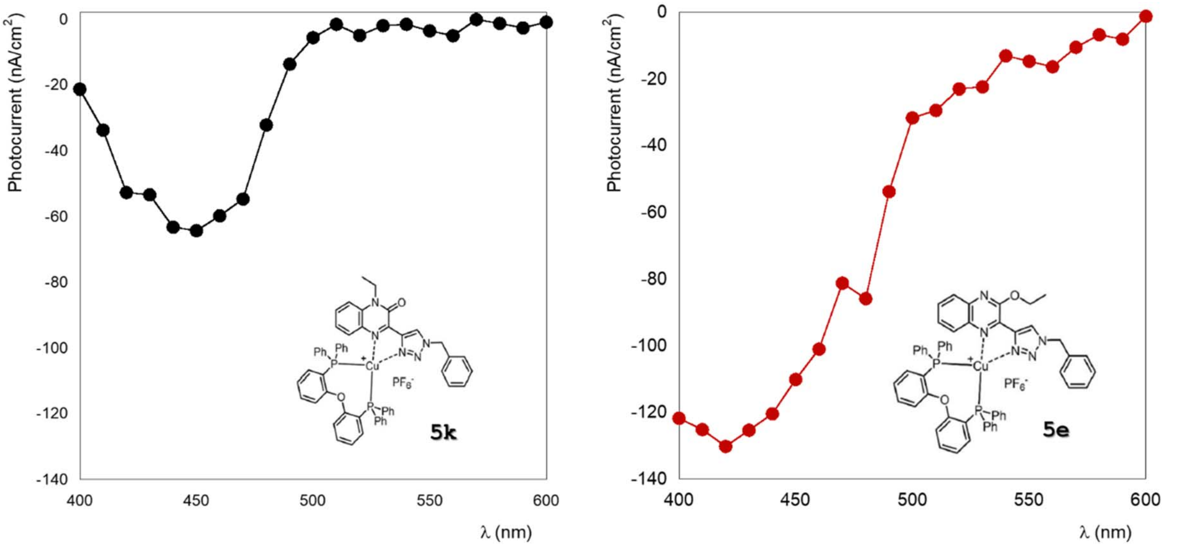

Fig. 9 Photocurrent action spectra of film **5k** (left) and **5e** (right) on TiO_2/FTO electrodes. The measurements were performed in an aqueous MV^{2+} solution, at 0 V (*vs.* Ag/AgCl), after photoirradiation at different wavelengths (every 10 nm from 400 to 600 nm).

been determined in TEOA solution, taking into account the measured pH value of this solution, that is 9.6.[62] When the driving force ($\Delta G°$) becomes very small, the rate constant for electron transfer decreases. In such systems, there is continuous competition between anodic and cathodic processes, which can be modulated by either adjusting the applied electrode potential or changing the electrolyte, thereby altering the redox potential of the medium.[63–65]

This effect has previously been demonstrated for zinc–tetraphenylporphyrin molecules on TiO_2 surfaces: when the redox potentials of the donor and acceptor are very close, the driving force for electron transfer is reduced, in accordance with Marcus theory.[66–68] As a consequence, the opposite process can dominate, a cathodic photocurrent, in which the dissolved oxygen present in the aqueous solution acts as the electron acceptor.

Since the energy level alignment of the two Cu(I) complexes predicts a negative (cathodic) photocurrent, we performed the same experiments in an aqueous solution containing an electron-accepting electrolyte, namely methyl viologen (MV^{2+}). Interestingly, in this electrolyte solution, the cathodic photocurrent intensity was approximately three times higher than that recorded in the presence of TEOA (Fig. 9). The TiO_2 region also produced a lower, yet still negative, photocurrent, indicating that a cathodic process occurs even on photoexcited TiO_2 particles. Even in this case, the conduction and valence band values of TiO_2 were calculated in the MV^{2+} solution, considering the different pH value of this solution, that is 6.5 (Fig. 10).

Furthermore, when comparing the visible-region response of complex **5k** with that of **5e**, we observed that the photocurrent obtained with **5e** was more than twice as high. This result further supports the role of the difference in redox potential between donor and acceptor species in governing the electron-transfer process: the larger potential gap in complex **5e** (0.55 V *vs.* 0.48 V, Fig. 10) enhances the driving force, in agreement with Marcus theory.

The incident photon-to-current efficiencies (IPCE%) calculated according to eqn (1) for the newly investigated compounds in methyl viologen solution are (0.005 ± 0.001) for complex **5k** and (0.013 ± 0.001) for complex **5e**.

To further enhance the photocurrent generation efficiency, experiments were conducted by varying the applied potential. Interestingly, upon applying a negative bias of −0.05 V, cathodic photocurrent densities of 230 nA cm^{-2} and 52 nA cm^{-2} were achieved for complexes **5e** and **5k**, respectively, when excited at 420 nm and 460 nm.

In the TEOA solution, tuning the applied potential allows a transition from cathodic to anodic photocurrent, even in the visible region where the Cu(I) complexes absorb. At an applied potential of +0.3 V, anodic photocurrent densities of 100 nA cm^{-2} and 80 nA cm^{-2} were recorded for complexes **5e** and **5k**, respectively, under excitation at the same wavelengths (460 and 420 nm, respectively).

These results highlight how the alignment of energy levels between the photoactive Cu(I) complexes, the TiO_2 substrate, and the redox electrolyte determines both the direction and magnitude of the photocurrent. When the edge of the TiO_2 conduction band lies at an energy favourable to electron injection from the excited complex, an anodic photocurrent is generated under UV irradiation in the presence of an electron donor. In contrast, when the excited-state oxidation potential of the complex is very close to the TiO_2 conduction band, the driving force for electron injection is reduced, leading to a cathodic photocurrent.

A comparison between complexes **5k** and **5e** reveals that **5e**, having a slightly higher excited-state redox potential (0.55 V *vs.* 0.48 V for **5k**), exhibits a stronger driving force for electron transfer and consequently generates a higher photocurrent response. This energetic distinction between the two complexes

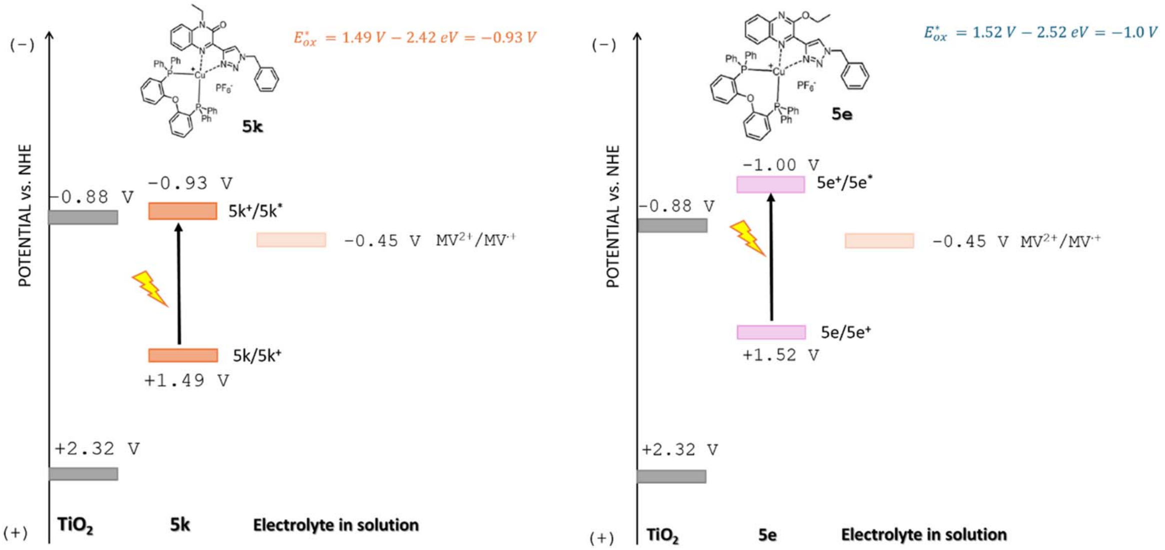

Fig. 10 Schematic representation of the energy levels involved in the photocurrent process in MV^{2+} solution, at pH = 6.5.

directly translates into their different photoelectrochemical behaviours under otherwise identical conditions. The possibility of **5e** having higher surface coverage can be excluded, since the same quantity of solution at the same concentration has been used for both dyes.

In summary, by exploring both anodic and cathodic regimes through variation of the donor/acceptor medium and the applied bias, we demonstrate the tunable photoelectrochemical behaviour of Cu(I)-based complexes anchored on TiO_2. The system incorporating **5e** consistently shows superior performance, producing cathodic photocurrents more than twice as high as those of **5k**, probably owing not only to its larger redox potential difference, which will favour the charge-transfer energetics, but also its longer excited-state lifetime may provide a role in its superior photoelectrochemical performance, giving a higher injection yield.

The threefold enhancement of cathodic photocurrent in methyl viologen solution, together with the polarity reversal to anodic photocurrent in TEOA under positive bias, emphasises the crucial influence of (i) the excited-state redox potential of the complex, (ii) the redox nature of the surrounding medium, and (iii) the applied potential at the electrode. Altogether, these findings demonstrate that the interplay between molecular design and interfacial energetics can be exploited to deliberately control the direction and efficiency of the photocurrent, a key step toward rational design of light-driven redox systems.

Conclusions

This study demonstrates that keto–enol tautomerism is a powerful synthetic strategy for accessing regioisomeric diimine ligands, which in turn lead to Cu(I) complexes with markedly different photophysical and electrochemical properties. The presence of a carbonyl group in complex **5k** introduces a stronger electrophilic character compared to the ethoxy substituent in **5e**, which acts as a moderate electron donor. These electronic differences significantly influence the metal-to-ligand charge transfer (MLCT) states, which are responsible for the lowest-energy absorption band extending up to 500 nm. Quantum-chemical calculations provided insight into the excited-state landscape, rationalising the peculiar photophysical behaviour observed. Both complexes are weakly emissive in solution, but exhibit intense red luminescence in the solid state. At low temperature, emission clearly originates from a triplet MLCT state; however, at room temperature, the occurrence of reverse intersystem crossing remains uncertain. The computed singlet-triplet energy gaps are rather in the upper range regarding TADF. However, **5k** features a local triplet excited (^{3}LE) state lying between the singlet and triplet MLCT states, potentially enabling a TADF-like mechanism. Finally, preliminary photoelectrochemical tests highlight the promising applicability of these complexes. When physisorbed on TiO_2 substrates, both compounds generate photocurrent under visible-light excitation, with excited-state redox potentials suitable for both anodic and cathodic regimes depending on the medium. Notably, upon 460 nm excitation, complex **5e** achieves a cathodic photocurrent density of 230 nA cm^{-2} using methyl viologen as electron acceptor—an impressive result considering the absence of anchoring groups. The ongoing work aims to introduce anchoring functionalities to further enhance the performance and stability in photoelectrocatalytic applications.

Experimental section

General information and materials

1,2-Phenylendiamine, iodoethane, methyl trifluoromethanesulfonate were commercially available. For the synthesis of 2-oxo-4-(triisopropylsilyl)but-3-ynoate a previously published procedure was followed. Further details on synthetic procedures are available on the SI file.

Synthetic procedures

3-(1′-Benzyl-1′*H*-1′,2′,3′-triazol-4′-yl)-1-ethylquinoxalin-2(1*H*)-one (4k). 1-Ethyl-3-ethynylquinoxalin-2(1*H*)-one (0.270 g, 1.36 mmol, 1.00 equiv.) was dissolved in 40 mL of a mixture of ethanol and water (7 : 3, v/v). Then the other reactants were added in the following order: sodium ascorbate (0.107 g, 0.54 mmol, 0.56 equiv), $CuSO_4 \cdot 5H_2O$ (0.069 g, 0.27 mmol, 0.20 equiv), sodium carbonate (0.056 mg, 0.68 mmol, 0.59 equiv), benzylazide (0.217 g, 1.63 mmol, 1.20 equiv). The mixture of reaction was left under stirring for two days. After this period of time, a solution of NH_4OH (10%) was added. The organic phase was extracted three times with dichloromethane, then it was washed with water (three times) and brine, dried over Na_2SO_4 and filtered. The product was purified *via* a precipitation, through addition of an excess of pentane to a concentrated dichloromethane solution of the compound, to obtain a yellow/ochre solid. (0.300 g, 0.91 mmol) yield: 67%. ^{1}H NMR (400 MHz, $CDCl_3$) δ = 8.72 (s, 1H, CH triazole), 8.16 (dd, J = 8.1, 1.5 Hz, 1H, H aromatic), 7.59–7.52 (m, 1H, H aromatic), 7.41–7.28 (m, 7H, H aromatic), 5.63 (s, 2H, C*H2*), 4.36 (q, J = 7.2 Hz, 2H, C*H2*), 1.38 (t, J = 7.2 Hz, 3H, C*H3*) ppm. ^{13}C NMR (101 MHz, $CDCl_3$) δ = 154.26, 143.15, 139.94, 138.90, 137.60, 134.66, 130.05, 129.67, 129.34, 129.01, 128.23, 127.10, 126.78, 126.36, 62.99, 54.41, 14.50 ppm. HRMS (ESI) *m*/*z* ($[M + H]^+$, ($C_{19}H_{17}N_5O$)): 332.1511 (calc), 332.1507 (found).

2-(1′-Benzyl-1′*H*-1′,2′,3′-triazol-4′-yl)-3-ethoxyquinoxaline (4e). 2-Ethoxy-3-ethynylquinoxaline (**3e**) (0.160 g, 0.80 mmol, 1.00 equiv.) was dissolved in 20 mL of a mixture of ethanol and water (7 : 3, v/v). Then the other reagents were added in the same order as in **4k**: sodium ascorbate (0.089 g, 0.45 mmol, 0.56 equiv), copper sulfate pentahydrate (0.040 g, 0.16 mmol, 0.20 equiv), sodium carbonate (0.039 mg, 0.47 mmol, 0.59 equiv), benzylazide (0.127 g, 0.95 mmol, 1.20 equiv). The procedure is the same as for ligand **4k**. A yellow ochre solid was obtained. (0.240 g, 0.72 mmol) Yield: 91%. ^{1}H NMR (400 MHz, $CDCl_3$) δ = 8.23 (d, J = 5.3 Hz, 2H, H aromatic), 7.81 (dd, J = 8.1, 1.5 Hz, 1H, H aromatic), 7.65 (ddd, J = 8.3, 6.9, 1.6 Hz, 1H, H aromatic), 7.58 (ddd, J = 8.4, 7.0, 1.5 Hz, 1H, H aromatic), 7.44–7.33 (m, 5H, H aromatic), 5.68 (s, 2H, C*H2*), 4.63 (q, J = 7.1 Hz, 2H, C*H2*), 1.46 (t, J = 7.1 Hz, 3H, C*H3*) ppm. ^{13}C NMR (101 MHz, $CDCl_3$) δ = 154.26, 143.15, 139.94, 138.90, 137.60, 134.66, 130.05, 129.68, 129.34, 129.01, 128.23, 127.10, 126.78, 126.36, 62.99, 54.41, 14.51 ppm. HRMS (ESI) *m*/*z* ($[M + H]^+$, ($C_{19}H_{17}N_5O$)): 332.1511 (calc), 332.1507 (found).

[Cu(I)(3-(1′-Benzyl-1′*H*-1′,2′,3′-triazol-4′-yl)-1-ethylquinoxalin-2(1*H*)-one)(bis[(2-diphenylphosphino)phenyl]ether)]PF_6 (5k). The synthesis of heteroleptic complexes was performed following already described procedures.[18] The complex **5k** was obtained as red crystals. (0.130 g, 0.12 mmol) Yield: 80%. ^{1}H NMR (400 MHz, CD_2Cl_2) δ = 8.65 (s, 1H, CH triazole), 7.78 (dd, J = 8.2, 1.4 Hz, 1H, H aromatic), 7.56–7.46 (m, 5H, H aromatic), 7.45–7.27 (m, 12H, H aromatic), 7.26–7.21 (m, 2H, H aromatic), 7.18 (t, J = 7.4 Hz, 2H, H aromatic), 7.06 (dtd, J = 8.3, 2.5, 1.1 Hz, 2H, H aromatic), 7.03–6.90 (m, 6H, H aromatic), 6.78 (dtd, J = 8.0, 4.2, 1.7 Hz, 2H, H aromatic), 6.75–6.65 (m, 4H, H aromatic), 6.63 (ddd, J = 8.3, 7.0, 1.3 Hz, 1H, H aromatic), 5.67 (s, 2H, C*H2*), 4.41 (q, J = 7.1 Hz, 2H, C*H2*), 1.41 (t, J = 7.1 Hz, 3H, C*H3*) ppm. ^{13}C NMR (101 MHz, CD_2Cl_2) δ = 158.90, 152.68, 134.85, 134.74, 134.06, 132.92, 132.72, 132.62, 132.20, 131.30, 131.08, 130.51, 130.03, 129.65, 129.62, 129.29, 128.79, 128.55, 128.28, 125.53, 124.13, 123.61, 123.46, 120.66, 114.52, 55.79, 38.56, 12.69 ppm. HRMS (ESI) *m*/*z* ($C_{55}H_{45}CuN_5O_2P_2^+$): 932.2345 (calc), 932.2325 (found). Elemental analysis $[C_{55}H_{45}CuN_5O_2F_6P_3] \cdot CH_2Cl_2$: C = 57.82, H = 4.07, N = 6.02 (calc); C = 58.12, H = 3.94, N = 6.30 (found).

[Cu(I)(2-(1′-Benzyl-1′*H*-1′,2′,3′-triazol-4′-yl)-3-ethoxyquinoxaline)(bis[(2-diphenylphosphino)phenyl]ether)]PF_6 (5e). The synthesis of heteroleptic complexes was performed following already described procedures.[18] The complex **5e** was obtained as orange crystals. (0.160 g, 0.14 mmol) Yield: 98%. ^{1}H NMR (400 MHz, CD_2Cl_2) δ = 8.28 (s, 1H, CH triazole), 7.77–7.68 (m, 2H, H aromatic), 7.44 (q, J = 6.7, 6.1 Hz, 5H, H aromatic), 7.33–7.16 (m, 13H, H aromatic), 7.07 (t, J = 7.4 Hz, 2H, H aromatic), 7.03–6.94 (m, J = 7.2 Hz, 3H, H aromatic), 6.88 (t, J = 7.5 Hz, 2H, H aromatic), 6.79 (dt, J = 16.2, 7.5 Hz, 5H, H aromatic), 6.67 (dtd, J = 8.0, 4.2, 1.7 Hz, 2H, H aromatic), 6.54–6.47 (m, 3H, H aromatic), 5.63 (s, 2H, C*H2*), 4.65 (q, J = 7.1 Hz, 2H, C*H2*), 1.46 (t, J = 7.1 Hz, 3H, C*H3*) ppm. ^{13}C NMR (101 MHz, CD_2Cl_2) δ 158.98, 154.65, 142.22, 141.38, 136.27, 134.82, 134.73, 134.65, 134.38, 132.49, 132.22, 132.14, 131.66, 131.16, 130.97, 130.66, 129.86, 129.54, 129.44, 129.23, 128.74, 128.49, 128.30, 127.49, 127.32, 127.21, 126.39, 125.42, 123.87, 123.71, 120.67, 64.53, 55.59, 14.51 ppm. HRMS (ESI) *m*/*z* ($C_{55}H_{45}CuN_5O_2P_2^+$): 932.2345 (calc), 932.2324 (found). Elemental analysis $[C_{55}H_{45}CuN_5O_2F_6P_3]$: C = 61.25, H = 4.21, N = 6.49 (calc); C = 61.21, H = 4.83, N = 5.96 (found).

Optical spectroscopy

UV-vis absorption spectra of solutions were recorded on a ALS SEC 2020 Wide wavelength range spectrometer using standard quartz cuvettes. Photoluminescence (PL) measurements were performed on Horiba Jobin Yvon Fluoromax and Fluorolog-322 spectrometers. Temperature-dependent spectra of solid (polycrystalline) samples were recorded using a closed-cycle optical cryostat operating between 3.2 and 300 K. Solutions were argon-purged before measurements. All emission spectra were corrected for the wavelength-dependent response of the spectrometer and detector (in relative photon flux units). Emission decay traces were recorded either by TCSPC technique with a pulsed laser diode excitation at 375 nm or by connecting the detector (photomultiplier) to a fast oscilloscope and applying a ns-pulsed nitrogen laser for excitation at 337 nm. PL quantum efficiencies of solid compounds were determined at ambient temperature with an integrating sphere out of optical PTFE, which was installed into the sample chamber of the spectrometer. The uncertainty of these measurements was estimated to be ±10%.

Electrochemical characterisation

The potentiostat Gamry Interface 1010B was connected to a three-electrodes electrochemical cell. The electrodes used are the following: glassy carbon disk (2 mm diameter) as the working electrode, a silver wire as the quasi-reference electrode and a platinum wire as the counter electrode. Electrochemical redox potentials were referred to the oxidation potential of ferrocene, used as internal standard. The measurements were carried out at room temperature, at different scan rates, typically the reported cyclic voltammetry were recorded at 100 mV s^{-1}. Concentrations of the analytes varied in the range between 2 and 5 mM, while the supporting electrolyte was tetrabutylammonium hexafluorophosphate ($TBAPF_6$) and its concentration was 0.1 M.

Quantum-chemical methods

All quantum-chemical calculations were done with the TURBOMOLE program package[69] using the Karlsruhe orbital basis sets of type def2-TZVP[70] and various standard density functionals (PBE0,[71] M06-2X[72]).

The structures of all investigated molecules were optimised using density functional theory (DFT) for electronic ground states and linear-response density functional theory (TDDFT) for electronic excited states. Geometry optimisations were done at the PBE0/TZVP level of theory, employing fine quadrature grids (size 5) and tight convergence criteria (SCF energy: 10^{-8} hartree, gradient: 10^{-5} hartree/bohr and inclusion of derivatives of quadrature weights). Vibrational frequencies for the electronic ground states were computed in order to ensure that the structures represent minima on the respective potential energy surface. Subsequent calculations of excitation energies were done based on these optimised geometries.

Excitation energies and oscillator strengths were calculated in the framework of linear-response density functional theory (TDDFT). We used the M06-2X/TZVP level of theory, fine quadrature grids (size 5) and tight convergence criteria (SCF energy: 10^{-8} hartree, one-electron density: 10^{-7}).

Deposition on TiO_2 surfaces

The two complexes were physiosorbed onto the TiO_2 glass. A solution of 0.2 mM in acetonitrile was used. The conductive substrates consisted of conductive FTO covered glass with a 0.25 cm^2 TiO_2 square. The deposition was performed by placing 20 μL of the solution onto the TiO_2 square and letting it dry for one hour before analysis. The deposited FTO glasses were dried under an argon flux.

Photocurrent generation measurements

Water was distilled and passed through a Milli-Q purification system. An aqueous 0.1 M sodium sulfate (Na_2SO_4) (Carlo Erba) solution was used as the electrolyte in photocurrent measurements to complete the electrical circuit of the electrochemical cell.

From the Na_2SO_4 solution, 50 mM triethanolamine (TEOA) (Sigma Aldrich) and methyl viologen (MV^{2+}) (Sigma Aldrich) solutions were prepared and used as a sacrificial electron donor or acceptor for regeneration of the dye.

Photocurrent measurements were performed at room temperature using a PG 310 potentiostat (Heka Elektronik) in a standard three-electrode configuration. The working electrode consisted of a conductive FTO glass substrate bearing a 0.25 cm^2 TiO_2 film onto which the two Cu(I) complexes were deposited. A platinum wire and an Ag/AgCl electrode were used as the counter and reference electrodes, respectively.

During the experiments, the electrodes were irradiated with a 150 W Xe lamp equipped with a monochromator, and the resulting photocurrent was recorded with the same potentiostat system. The incident photon-to-current efficiency (IPCE) was calculated according to eqn (1).

$$\mathrm{IPCE}\ (\%) = \frac{100 \times i(\mathrm{A/cm^2}) \times 1240}{I(\mathrm{W/cm^2}) \times \lambda(\mathrm{nm})} \tag{1}$$

where i is the measured photocurrent, I is the incident light power density, and λ is the incident wavelength (340 nm). The intensity of the incident light was evaluated with a Vector H410 Power Meter (Scientech, USA).

The redox potentials of the excited state have been calculated using the following equations:

$$E^0(\mathrm{A^+/A^*}) = E^0(\mathrm{A^+/A}) - E_{00}(\mathrm{A^*/A}) \tag{2}$$

$$E^0(\mathrm{A^*/A^-}) = E^0(\mathrm{A/A^-}) - E_{00}(\mathrm{A/A^*}) \tag{3}$$

where E^0 (A^+/A^*) and E^0 (A^*/A^-) are respectively, the excited state redox potential of oxidation and reduction of a redox species, and where E_{00} is the energy difference between the ground state and the excited state, determined spectroscopically.[61]

The potentials of the **5k** and **5e** complexes have been evaluated *vs.* NHE reference electrodes, by adding the value of 0.64 V.[59,73]

Author contributions

CeBr carried out the synthesis of the ligands and the final complexes. CeBr and CB characterised the complexes electrochemically and photophysically at room temperature in organic solution. DG and SL carried out the photophysics in solid state and at low temperature. OF solved the molecular structures. VC, RL and EG performed photoelectrochemical experiments. AB performed the quantum-chemical calculations. CB acquired fundings and coordinated the project. The manuscript was written through contributions of all authors. All authors have given approval to the final version of the manuscript.

Conflicts of interest

There are no conflicts to declare.

Data availability

The data supporting this article have been included as part of the Supplementary Information (SI). Supplementary information is available. See DOI: https://doi.org/10.1039/d6ta00742b.

CCDC 2495572–2495575 contain the supplementary crystallographic data for this paper.[74–77]

Acknowledgements

Prof. Stefan Bräse from the Institute of Organic Chemistry at the Karlsruhe Institute of Technology (KIT) is gratefully acknowledged for lab space and instrumentation. We thank Tilman Köhler (KIT) for synthetic support and reproducing the synthetic procedures. Dr Luigi Vesce and Prof. Aldo Di Carlo from the Department of Engineering of the University of Rome Tor Vergata are kindly acknowledged for providing the TiO_2 substrates. Open access supported by an open access agreement between KIT and the Royal Society of Chemistry.

Notes and references

1 C. Förster and K. Heinze, *Chem. Soc. Rev.*, 2020, **49**, 1057–1070.
2 O. S. Wenger, *J. Am. Chem. Soc.*, 2018, **140**, 13522–13533.
3 V. Ferraro, C. Bizzarri and S. Bräse, *Advanced Science*, 2024, 2404866.
4 M. A. Bryden and E. Zysman-Colman, *Chem. Soc. Rev.*, 2021, **50**, 7587–7680.
5 L. Hämmerling and E. Zysman-Colman, *Chem Catal.*, 2024, **4**, 101061, DOI: 10.1016/j.checat.2024.101061.
6 F. N. Castellano and M. C. Rosko, *Acc. Chem. Res.*, 2024, **57**, 2872–2886.
7 M. S. Lazorski and F. N. Castellano, *Polyhedron*, 2014, **82**, 57–70.
8 M. C. Rosko, J. P. Wheeler, R. Alameh, A. P. Faulkner, N. Durand and F. N. Castellano, *Inorg. Chem.*, 2024, **63**, 1692–1701.
9 C. Bruschi, X. Gui, O. Fuhr, W. Klopper and C. Bizzarri, *Dalton Trans.*, 2023, **52**, 7809–7818.
10 N. Vlachopoulos, M. Freitag and A. Hagfeldt, in *Counter Electrodes for Dye-sensitized and Perovskite Solar Cells*, 2018, pp. 349–365, DOI: 10.1002/9783527813636.ch14.
11 A. Colombo, C. Dragonetti, M. Magni, D. Roberto, F. Demartin, S. Caramori and C. A. Bignozzi, *ACS Appl. Mater. Interfaces*, 2014, **6**, 13945–13955.
12 L. E. Burmeister, F. Doettinger, K. J. Haseloff, C. Kleeberg, M. Boujtita, S. Pascal, F. Odobel, S. Tschierlei, Y. Pellegrin and M. Karnahl, *JACS Au*, 2025, **5**, 3960–3973.
13 M. Sandroni, Y. Pellegrin and F. Odobel, *C. R. Chim.*, 2016, **19**, 79–93.
14 M. Jilakian and T. H. Ghaddar, *ACS Appl. Energy Mater.*, 2022, **5**, 257–265.
15 T. Higashino, H. Iiyama, S. Nimura, Y. Kurumisawa and H. Imahori, *Inorg. Chem.*, 2020, **59**, 452–459.
16 E. Tanaka, H. Michaels, M. Freitag and N. Robertson, *J. Mater. Chem. A*, 2020, **8**, 1279–1287.
17 C. Minozzi, A. Caron, J.-C. Grenier-Petel, J. Santandrea and S. K. Collins, *Angew. Chem., Int. Ed.*, 2018, **57**, 5477–5481.
18 C. Bruschi, X. Gui, N. Salaeh-arae, T. Barchi, O. Fuhr, S. Lebedkin, W. Klopper and C. Bizzarri, *Eur. J. Inorg. Chem.*, 2021, **2021**, 4074–4084.
19 S. Engl and O. Reiser, *ACS Catal.*, 2020, **10**, 9899–9906.
20 S. Engl and O. Reiser, *Eur. J. Org Chem.*, 2020, **2020**, 1523–1533.
21 T. Mandal, N. Katta, H. Paps and O. Reiser, *ACS Org. Inorg. Au*, 2023, **3**, 171–176.
22 S. Paria and O. Reiser, *ChemCatChem*, 2014, **6**, 2477–2483.
23 Y. Yang, C. Zhang, C. Zhang, Y. Shi, J. Li, B. Johannessen, Y. Liang, S. Zhang, Q. Song, H. Zhang, J. Huang, J. Ke, L. Zhang, Q. Song, J. Zeng, Y. Zhang, Z. Geng, P.-S. Wang, Z. Wang, J. Zeng and F. Li, *Nat. Commun.*, 2024, **15**, 6316.
24 V. Leandri, A. R. P. Pizzichetti, B. Xu, D. Franchi, W. Zhang, I. Benesperi, M. Freitag, L. Sun, L. Kloo and J. M. Gardner, *Inorg. Chem.*, 2019, **58**, 12167–12177.
25 J. Beaudelot, G. Evano and C. Moucheron, *Chem. – Eur. J.*, 2023, **29**, e202300758.
26 F. Doettinger, Y. Yang, M. Karnahl and S. Tschierlei, *Inorg. Chem.*, 2023, **62**, 8166–8178.
27 L. Gimeno, C. Queffelec, E. Blart and Y. Pellegrin, *ACS Omega*, 2022, **7**, 13112–13119.
28 T. Hosono, N. O. Decarli, P. Z. Crocomo, T. Goya, L. E. de Sousa, N. Tohnai, S. Minakata, P. de Silva, P. Data and Y. Takeda, *J. Mater. Chem. C*, 2022, **10**, 4905–4913.
29 M. K. Etherington, F. Franchello, J. Gibson, T. Northey, J. Santos, J. S. Ward, H. F. Higginbotham, P. Data, A. Kurowska, P. L. Dos Santos, D. R. Graves, A. S. Batsanov, F. B. Dias, M. R. Bryce, T. J. Penfold and A. P. Monkman, *Nat. Commun.*, 2017, **8**, 14987.
30 T. Silies, S. Tombolato, D. Stappers, N. L. Doltsinis, C. G. Daniliuc and F. Rizzo, *ChemistryEurope*, 2025, **3**, e202400085.
31 M. Schmiedtchen, I. Maisuls, C. Wölper, C. A. Strassert and J. Voskuhl, *ChemPhotoChem*, 2024, **8**, e202300209.
32 B. Roy, I. Maisuls, J. Zhang, F. C. Niemeyer, F. Rizzo, C. Wölper, C. G. Daniliuc, B. Z. Tang, C. A. Strassert and J. Voskuhl, *Angew. Chem., Int. Ed.*, 2022, **61**, e202111805.
33 X. Hu, H. Chen, L. Zhao, M. Miao and Y. Zheng, *Chem. Mater.*, 2019, **31**, 10256–10262.
34 T. Wang, M. Li, Y. Chen, X. Che, F. Bi, Y. Yang, R. Yang and C. Li, *ACS Catal.*, 2023, **13**, 15439–15447.
35 Y. Xiang, X. Wang, L. Rao, P. Wang, D. Huang, X. Ding, X. Zhang, S. Wang, H. Chen and Y. Zhu, *ACS Energy Lett.*, 2018, **3**, 2544–2549.
36 S. Malagón del Molino, M. Schmiedtchen, C. Mück-Lichtenfeld, J. Voskuhl and O. García Mancheño, *Eur. J. Org Chem.*, 2025, e202500873.
37 C. Bizzarri, A. P. Arndt, S. Kohaut, K. Fink and M. Nieger, *J. Organomet. Chem.*, 2018, **871**, 140–149.
38 L.-L. Gracia, L. Luci, C. Bruschi, L. Sambri, P. Weis, O. Fuhr and C. Bizzarri, *Chem. – Eur. J.*, 2020, **26**, 9929–9937.
39 E. González-Fernández, N. Marinus, J. Dhankhar, A. Linden and I. Čorić, *Chem. – Eur. J.*, 2024, **30**, e202401215.
40 N. Arnosti, M. Meyer, A. Prescimone, E. C. Constable and C. E. Housecroft, *Crystals*, 2021, **11**, 185.
41 S. Wang, E. E. Morgan, S. Panuganti, L. Mao, P. Vishnoi, G. Wu, Q. Liu, M. G. Kanatzidis, R. D. Schaller and R. Seshadri, *Chem. Mater.*, 2022, **34**, 3206–3216.
42 X. Liu, R. Li, L. Ma, X. Feng and Y. Ding, *New J. Chem.*, 2016, **40**, 619–625.
43 M. Grupe, P. Boden, P. Di Martino-Fumo, X. Gui, C. Bruschi, R. Israil, M. Schmitt, M. Nieger, M. Gerhards, W. Klopper,

C. Riehn, C. Bizzarri and R. Diller, *Chem. – Eur. J.*, 2021, **27**, 15252–15271.

44 Z. Zhao, S. Liu, S. Cui, Y. Zhang, Z. Jiang and X. Li, *Molecules*, 2025, **30**, 3973.

45 I. García-Orozco, J. G. López-Cortés, M. C. Ortega-Alfaro, R. A. Toscano, G. Penieres-Carrillo and C. Alvarez-Toledano, *Inorg. Chem.*, 2004, **43**, 8572–8576.

46 M. Vargas-Zamarripa, J. M. González, O. Carreño-Vega, E. D. Cervantes, O. Serrano and G. R. García, *J. Photochem. Photobiol., A*, 2026, **470**, 116636.

47 T. Karasawa, R. Oriez, N. Kumagai and M. Shibasaki, *J. Am. Chem. Soc.*, 2018, **140**, 12290–12295.

48 B. D. Lindner, Y. Zhang, S. Höfle, N. Berger, C. Teusch, M. Jesper, K. I. Hardcastle, X. Qian, U. Lemmer, A. Colsmann, U. H. F. Bunz and M. Hamburger, *J. Mater. Chem. C*, 2013, **1**, 5718–5724.

49 F. Himo, T. Lovell, R. Hilgraf, V. V. Rostovtsev, L. Noodleman, K. B. Sharpless and V. V. Fokin, *J. Am. Chem. Soc.*, 2005, **127**, 210–216.

50 R. Czerwieniec, M. J. Leitl, H. H. H. Homeier and H. Yersin, *Coord. Chem. Rev.*, 2016, **325**, 2–28.

51 J. M. Busch, D. M. Zink, P. Di Martino-Fumo, F. R. Rehak, P. Boden, S. Steiger, O. Fuhr, M. Nieger, W. Klopper, M. Gerhards and S. Bräse, *Dalton Trans.*, 2019, **48**, 15687–15698.

52 R. Czerwieniec and H. Yersin, *Inorg. Chem.*, 2015, **54**, 4322–4327.

53 M. J. Leitl, D. M. Zink, A. Schinabeck, T. Baumann, D. Volz and H. Yersin, in *Photoluminescent Materials and Electroluminescent Devices*, eds. N. Armaroli and H. J. Bolink, Springer International Publishing, Cham, 2017, pp. 141–174, DOI: 10.1007/978-3-319-59304-3_5.

54 H. Yersin and U. Monkowius, *Adv. Photonics Res.*, 2025, **6**, 2400111.

55 X. Gui, C. Holzer and W. Klopper, *J. Chem. Theory Comput.*, 2018, **14**, 2127–2136.

56 M. K. Etherington, J. Gibson, H. F. Higginbotham, T. J. Penfold and A. P. Monkman, *Nat. Commun.*, 2016, **7**, 13680.

57 J. Gibson, A. P. Monkman and T. J. Penfold, *ChemPhysChem*, 2016, **17**, 2956–2961.

58 J. P. Zobel, A. M. Wernbacher and L. González, *Angew. Chem., Int. Ed.*, 2023, **62**, e202217620.

59 R. R. Gagne, C. A. Koval and G. C. Lisensky, *Inorg. Chem.*, 1980, **19**, 2854–2855.

60 C. M. Cardona, W. Li, A. E. Kaifer, D. Stockdale and G. C. Bazan, *Adv. Mater.*, 2011, **23**, 2367–2371.

61 P. Makuła, M. Pacia and W. Macyk, *J. Phys. Chem. Lett.*, 2018, **9**, 6814–6817.

62 V. V. Matylitsky, M. O. Lenz and J. Wachtveitl, *J. Phys. Chem. B*, 2006, **110**, 8372–8379.

63 S. Yasutomi, T. Morita, Y. Imanishi and S. Kimura, *Science*, 2004, **304**, 1944–1947.

64 M. Venanzi, E. Gatto, M. Caruso, A. Porchetta, F. Formaggio and C. Toniolo, *J. Phys. Chem. A*, 2014, **118**, 6674–6684.

65 K. Yanagisawa, T. Morita and S. Kimura, *J. Am. Chem. Soc.*, 2004, **126**, 12780–12781.

66 E. Gatto, S. Kubitzky, M. Schriever, S. Cesaroni, C. Mazzuca, G. Marafon, M. Venanzi and M. De Zotti, *Angew. Chem., Int. Ed.*, 2019, **58**, 7308–7312.

67 S. Kubitzky, R. Lettieri, E. Passaretti, M. Venanzi, M. De Zotti, C. Mazzuca, E. Placidi and E. Gatto, *Adv. Mater. Interfaces*, 2025, **12**, 2400418.

68 S. Kubitzky, M. Venanzi, B. Biondi, R. Lettieri, M. De Zotti and E. Gatto, *Chem. - Eur. J.*, 2021, **27**, 2810–2817.

69 TURBOMOLE V7.6 (2021), *a Development of University of Karlsruhe and Forschungszentrum Karlsruhe GmbH 1989–2007*, TURBOMOLE GmbH since 2007; available from https://www.turbomole.org.

70 F. Weigend and R. Ahlrichs, *Phys. Chem. Chem. Phys.*, 2005, **7**, 3297–3305.

71 J. P. Perdew, M. Ernzerhof and K. Burke, *J. Chem. Phys.*, 1996, **105**, 9982–9985.

72 Y. Zhao and D. G. Truhlar, *Acc. Chem. Res.*, 2008, **41**, 157–167.

73 D. Nieto, S. Bruña, M. M. Montero-Campillo, J. Perles, A. M. a. González-Vadillo, J. Méndez, O. Mo and I. Cuadrado, *Chem. Commun.*, 2013, **49**, 9785–9787.

74 CCDC 2495572: Experimental Crystal Structure Determination, 2026, DOI: 10.5517/ccdc.csd.cc2prvbn.

75 CCDC 2495573: Experimental Crystal Structure Determination, 2026, DOI: 10.5517/ccdc.csd.cc2prvcp.

76 CCDC 2495574: Experimental Crystal Structure Determination, 2026, DOI: 10.5517/ccdc.csd.cc2prvdq.

77 CCDC 2495575: Experimental Crystal Structure Determination, 2026, DOI: 10.5517/ccdc.csd.cc2prvfr.